

MIT Open Access Articles

*High-Strain-Rate Behavior of a Viscoelastic
Gel Under High-Velocity Microparticle Impact*

The MIT Faculty has made this article openly available. **Please share**
how this access benefits you. Your story matters.

As Published: <https://doi.org/10.1007/s11340-020-00639-9>

Publisher: Springer US

Persistent URL: <https://hdl.handle.net/1721.1/131931>

Version: Author's final manuscript: final author's manuscript post peer review, without publisher's formatting or copy editing

Terms of use: Creative Commons Attribution-Noncommercial-Share Alike



High-strain-rate behavior of a viscoelastic gel under high-velocity microparticle impact

Cite this article as: D. Veysset, Y. Sun, J. Lem, S. E. Kooi, A. A. Maznev, S. T. Cole, R. A. Mrozek, J. L. Lenhart, K. A. Nelson., High-strain-rate behavior of a viscoelastic gel under high-velocity microparticle impact, *Experimental Mechanics*, doi: [10.1007/s11340-020-00639-9](https://doi.org/10.1007/s11340-020-00639-9)

This Author Accepted Manuscript is a PDF file of a an unedited peer-reviewed manuscript that has been accepted for publication but has not been copyedited or corrected. The official version of record that is published in the journal is kept up to date and so may therefore differ from this version.

Terms of use and reuse: academic research for non-commercial purposes, see here for full terms. <http://www.springer.com/gb/open-access/authors-rights/aam-terms-v1>

Author accepted manuscript

High-strain-rate behavior of a viscoelastic gel under high-velocity microparticle impact

D. Veysset^{a,*}, Y. Sun^{a,b}, J. Lem^{a,b}, S. E. Kooi^a, A. A. Maznev^{a,b}, S. T. Cole^c, R. A. Mrozek^c, J. L. Lenhart^c,
K. A. Nelson^{a,b}.

^aInstitute for Soldier Nanotechnologies, MIT, Cambridge, Massachusetts 02139, USA

^bDepartment of Chemistry, MIT, Cambridge, Massachusetts 02139, USA

^cU.S. Army Research Laboratory, CCDC ARL, Aberdeen Proving Ground, MD 21005-5069;

*Correspondence to the author. E-mail address: dveysset@mit.edu (D. Veysset)

Abstract

Background: Impact experiments, routinely performed at the macroscale, have long been used to study mechanical properties of materials. Microscale high-velocity impact, relevant to applications such as ballistic drug delivery has remained largely unexplored at the level of a single impact event. **Objective:** In this work, we study the mechanical behavior of polymer gels subjected to high-velocity microparticle impact, with strain rates up to 10^7 s^{-1} , through direct visualization of the impact dynamics. **Methods:** In an all-optical laser-induced particle impact test, 10–24 μm diameter steel microparticles are accelerated through a laser ablation process to velocities ranging from 50 to 1000 m/s. Impact events are monitored using a high-speed multi-frame camera with nanosecond time resolution. **Results:** We measure microparticle trajectories and extract both maximum and final penetration depths for a range of particle sizes, velocities, and gel concentrations. We propose a modified Clift-Gauvin model and demonstrate that it adequately describes both individual trajectories and penetration depths. The model parameters, namely, the apparent viscosity and impact resistance, are extracted for a range of polymer concentrations. **Conclusions:** Laser-induced microparticle impact test makes it possible to perform reproducible measurements of the single particle impact dynamics on gels and provides a quantitative basis for understanding these dynamics. We show that the modified Clift-Gauvin model, which accounts for the velocity dependence of the drag coefficient, offers a better agreement with the experimental data than the more commonly-used Poncelet model. Microscale ballistic impact

imaging performed with high temporal and spatial resolution can serve as direct input for simulations of high-velocity impact responses and high strain rate deformation in gels and other soft materials.

Keywords: viscoelastic gels; high strain rate; high-velocity impact; penetration; high-speed imaging.

Introduction

Understanding the high-strain-rate behavior of materials under microscale impact is important for many engineering applications, such as the spacecraft protection against micro-meteorites [1, 2], sand erosion of pipelines [3] and helicopter rotor blades [4, 5], impact bonding for additive manufacturing [6], and needle-free drug delivery [7]. Many materials involved in these applications possess rate-dependent properties that need to be understood for effective engineering use. The knowledge of rate-dependent mechanical properties of soft materials, such as hydrogels and biological tissues, will help interpret impact injuries [8–10] and predict the collateral tissue damage that may occur during lithotripsy [11] or other ultrasound- and laser-based surgical procedures [12, 13], where strain rates above 10^5 s^{-1} can be reached. However, quantitative characterization remains a challenge as few experimental tools can probe soft material behaviors beyond strain rates of 10^3 s^{-1} .

The most common technique used for high-strain-rate measurements of materials, the Split-Hopkinson Pressure Bar (SHPB), faces difficulties in testing soft materials because of low material strength, stiffness and impedance, and has difficulty in reaching stress equilibrium owing to low wave velocity [14–16]. Plate impact experiments, despite their wide use for metallic, ceramic, polymeric or composite materials, have rarely been employed to study the high-rate behavior of gels [17]. A more recent technique, the laser-induced cavitation (LIC) method, tailored for soft materials, allows non-contact, local, micro-rheology measurements at ultra-high strain rates [18]. In a typical LIC experiment, a laser pulse is focused inside a transparent soft material, e.g., a hydrogel, causing a bubble to nucleate and quickly expand thus straining the surrounding material at strain rates up to 10^8 s^{-1} . The bubble dynamics can be observed in real-time using, for instance, high-speed photography and viscoelastic properties can be inferred from the bubble dynamics. This method is particularly appropriate for studying traumatic brain injuries, where tissue damage has been suggested to result from shock-induced cavitation [19]. This technique nonetheless requires the sample to absorb the laser radiation

while being transparent to the imaging light and does not isolate the laser-induced thermal response from the purely mechanical response [20]. In contrast, the laser-induced particle impact test (LIPIT) [21, 22], which can launch microparticles to supersonic velocities, is well suited for studying high-rate deformations relevant to micro-impacts applications. For instance, the LIPIT apparatus has recently been used to investigate a variety of impact behaviors including impact bonding and impact erosion of metals [23–27], dynamic stiffening of elastomers [22, 28–31], perforation of thin films [32–34], and penetration in gelatin [35].

In this work, we use LIPIT to study high-velocity microparticle impact on synthetic polymer gels containing a non-aqueous solvent. We accelerate steel microparticles to velocities ranging from 50 to 1000 m/s, corresponding to characteristic strain rates, estimated as v/D [36], up to $\sim 10^7$ s⁻¹ and observe particle penetration and gel deformation in real time via ultra-high-speed imaging. We analyze a large number of individual microparticle trajectories and obtain the penetration depth as a function of the impact velocity for a range of the gel concentration. The results are analyzed with the help of the Clift-Gauvin model [37] modified for yield-stress fluids.

Materials and methods

Sample preparation

Polymer gels were prepared as previously reported [38]. Poly(styrene-*b*-ethylene-*co*-butylene-*b*-ethylene) (G1652; Kraton Polymers LLC) powder was mixed with light mineral oil (obtained from McMaster Carr) at the ratios required to obtain 15, 20, 25, 30, and 40 vol% polymer, respectively. The mixture was heated to 120 °C for 8 h stirring intermittently to melt and dissolve the polymer in the mineral oil. The melts were cast into glass petri dishes and held at 120 °C for 8 h to remove the air bubbles incorporated during mixing. The molds were cooled to room temperature, resulting in phase separation and aggregation of the polystyrene chain ends to form a physically cross-linked polymer network. The obtained gel densities are listed in Table 1.

Table 1. Gel sample densities.

Polymer concentration C (vol%)	15	20	25	30	40
Density ρ_s (kg/m ³)	861	864	867	870	875

Microparticle impact test

Figure 1 shows a schematic of the LIPIT apparatus. The assembly from which particles were launched (hereafter referred to as the launch pad) consists of a glass substrate (25-mm diameter, 210- μm thickness), a gold layer (60-nm thickness) and a polyurea film (30- μm thickness). Details regarding the fabrication of the launch pad can be found in Refs [23, 39]. Steel particles (Cospheric, diameters D varying from 10 to 24 μm , density $\rho_p = 7800 \text{ kg/m}^3$) were sparsely spread on the launch pad using a lens-cleaning paper and a drop of ethanol. Particles were accelerated following ablation of the gold film by a laser pulse (Nd-YAG, 532-nm wavelength, 10-ns duration, 50- μm focal spot size). A charge-coupled device (CCD) camera was used to view the launch pad, select a particle, measure its size, and position it at the focus of the laser beam before launch. A microscope objective (10 \times) and a tube lens (40-cm focal length) imaged the impact plane onto a high-speed camera (SIMX16, Specialised Imaging), with a field of view of 400 \times 300 μm and a resolution of 1280 \times 960 pixels. The camera provides 16 frames with a maximum frame rate of 300 million fps. A diode laser pulse (532-nm wavelength, 30- μs duration, Cavilux Smart, Cavitar) was used for illumination. The gel samples were cut to yield 15-mm tall, 15-mm wide, and 2-mm thick targets. The specimens were positioned so that the impacts occurred 300 μm from the edge facing the microscope objective, a distance greatly exceeding the particle diameter. We therefore assume that the target can be effectively considered semi-infinite.

Two representative image sequences of steel particle impacts are shown in Fig. 2. The particles were imaged in air before impact to measure the impact velocity, with a 2% uncertainty. In both cases, the particle fully penetrated in the gel after impact. A cavity behind the particle rapidly evolved into a conical shape for the first impact at 215 m/s and into a “carrot” shape for the second impact at 630 m/s. Subsequently, the cavity closed and the particle was pushed back toward the surface to its final residual penetration depth (P_{res}) after reaching a maximum penetration depth (P_{max}).

Results and discussion

Impact trajectories and maximum penetrations

Figure 3a shows particle penetration trajectories for three representative impacts on the 40% gel, including both impacts shown in Fig. 2. Normalized maximum (P_{max}/D) and residual (P_{res}/D) penetration depths obtained from 45 individual trajectories are plotted in Fig. 3b versus the impact velocity. The penetration depth was measured as the distance between the target surface before impact and the particle position plus the particle radius (the “nose contribution”) at the maximum penetration as well as in the final state (the residual penetration). The particle size is indicated by the color of the data points in Fig. 3b, with smaller particles generally yielding higher impact velocities. The error in the particle diameter measurements was the same ($\pm 1 \mu\text{m}$) for all particles; therefore larger normalized penetration depth errors are reported for smaller particles.

The rich information contained in the cavity dynamics imaged with high temporal and spatial resolutions in addition to particle trajectories can be used to calibrate materials models for high-rate deformations [40, 41]. The elastic recoil has been observed previously for macroscale particle impact on viscoelastic gels [42]. The elastic recoil, arising from the solid character of the gel, and the sample recovery (or healing) occurring at longer time scales are not the subject of the present work as we here are interested in the high strain rate response. This behavior is worthy of future investigation as the recoil motion is not yet fully understood [42].

Modified Clift-Gauvin model for particle penetration

To model the trajectories and calculate the maximum penetration depth, we assume our materials to behave as yield-stress fluids. Under the Bingham plastic assumption, when mechanical stresses exceed a yield strength, the material transitions from a solid-like behavior to a Newtonian fluid-like behavior [43]. The yield-stress model has been used to describe particle motion in viscoelastic fluids such as aqueous foams, clay suspensions, granular media, gelatin, or polymer gels [36, 44–47]. Under this assumption, the total drag force F acting on the particle as it penetrates the gel can be represented as a sum of three components: inertial (F_i) and viscous (F_v) forces related to the Newtonian behavior and an additional yield resistance (F_y) force. The drag coefficient, defined as $C_D = F/(Av^2/2)$ where A the cross-sectional area of the particle, depends on the Reynolds number, with $Re = \rho_s vL/\eta$, where ρ_s is the density of the medium, v is the velocity of the particle,

L is the characteristic dimension of the particle (taken as the particle diameter D), and η is the dynamic viscosity. For Newtonian fluids, the drag coefficient is relatively constant at high Reynolds numbers ($10^3 < Re < 10^5$, also called Newton's regime) where inertial stresses dominate with $C_{D,inertial} = F_i / (Av^2/2) \cong 0.5$ [37]. At lower Reynolds number ($Re < 100$), where viscous stresses dominate over inertial stresses, the drag coefficient is determined by the Stokes' law with $C_{D,viscous} = F_v / (Av^2/2) = 24/Re$. As the velocity of the particle further decreases, the yield resistance force F_y finally dominates. This force decomposition approach has been recently used by Liu et al. to describe projectile penetration in gelatin, assuming a strain-rate-dependent yield resistance force [36].

Furthermore, between the Stokes' and Newton's regimes lies a transitional regime ($10^2 < Re < 10^3$). Taking into account the transitional regime, Clift and Gauvin proposed the following empirical form for C_D [37],

$$C_D^{C-G} = \frac{24}{Re} (1 + 0.15Re^{0.687}) + \frac{0.42}{1 + 4.25 \times 10^4 Re^{-1.16}}, \quad (1)$$

accounting for the inertial and viscous forces and has proven valid for fluids for Reynolds numbers up to 10^5 [48]. This drag form reduces, as expected, to $C_{D,viscous}$ at low Re and $C_{D,inertial}$ at high Re . Assuming *a priori* that Reynolds numbers in our experiments are lower than 10^5 , we opted to use this drag description for the combined contribution of F_i and F_v . In our modified Clift-Gauvin model, the total force is therefore expressed as:

$$F = \frac{1}{2} C_D^{C-G} \rho_s A v^2 + AR. \quad (2)$$

The validity of this assumption ($Re < 10^5$) will be verified *a posteriori*. In addition, we assumed a constant viscosity and a constant yield resistance termed R . In our experiments, the contributions of surface tension and gravity to the drag force can be neglected. The characteristic Weber number, $We = \rho_s v^2 L / \sigma$, where σ is the surface tension, indicates the relative importance of inertia and surface tension. Taking an approximate surface tension of 10^{-2} N/m, typical for soft gels [49, 50], and with $\rho_s \sim 1000$ kg/m³, $v \sim 1000$ m/s, $L \sim 10$ μ m, the Weber number in our experimental conditions is about 10^6 . The Froude number, $Fr = v^2 / gL$, where g is the standard gravity, which indicates the ratio of the inertial force to the gravity force, is about 10^{10} .

By numerically solving the equation of motion using Eq. 2, we simulate the trajectories and find the maximum penetration depth. The apparent viscosity η and resistance R are treated as fitting parameters whose values are determined from the best fit to the maximal penetration data shown in Fig. 4. Details regarding the fitting procedure can be found in the supplementary information (Figs. S1-2). The viscosity was found to be 4.5×10^{-2} Pa.s ($\pm 1.0 \times 10^{-2}$ Pa.s) and the resistance 25 MPa (± 5 MPa). Based on the obtained viscosity value, the maximum Reynolds number in our experiments is of the order of 500, well within the validity range of Eq. (1). Above 200 m/s, we note a good agreement in the calculated maximum penetrations up to the maximum tested velocity of ~ 800 m/s, which supports the modified Clift-Gauvin model. We verified that the model also reproduces the individual trajectories, as shown in Fig. 3a. At lower velocities, below 200 m/s, the model deviates from the experimental data, underpredicting the penetration depth by about one particle radius (see Fig. S3 for percent deviation). This can be explained by the fact that the model ignores surface effects, which become increasingly important at low velocities (as the Weber number approaches unity) where the particle does not penetrate deeply into the gel.

Comparison with the Poncelet model

High-velocity penetration trajectories in gel materials have also been described using a Poncelet model, often for high-velocity impact on gelatins, with reasonable success [35, 40, 51, 52]. In this model, the expression for the force acting on the particle consists of only two terms, the inertial drag term and the resistance term, neglecting the viscous term contribution [53–55]:

$$F_{Poncelet} = \frac{1}{2} C_D \rho_s A v^2 + AR, \quad (3)$$

where C_D is taken as a constant, in contrast to the modified Clift-Gauvin model where C_D is velocity dependent. Importantly, the Poncelet model implicitly assumes the Reynolds number to be above $\sim 10^3$. In macroscale ballistic impact studies, the Reynolds number is typically larger than 10^3 , hence the assumption of a constant drag coefficient C_D is reasonable. The Poncelet model yields the following analytical solution for the maximum penetration,

$$P_{max,Poncelet} = \frac{2}{3} \frac{\rho_p D}{\rho_s C_D} \ln \left(\frac{\rho_s C_D v_0^2}{2R} + 1 \right). \quad (4)$$

In Fig. 4, a fit to the experimental data with Eq. 4 is shown alongside the fit by the modified Clift-Gauvin model. The best fit parameters in Eq. 4 are $C_D = 1.5 (\pm 0.1)$ and $R = 21 \text{ MPa} (\pm 5 \text{ MPa})$. While the value for R is similar to what was obtained with Eq. 2 (within the fit error), the value for C_D would correspond to a Reynolds number of ~ 50 for Newtonian fluids, indicating that the viscosity cannot be neglected. Consequently, the Poncelet model assumption ($Re > 10^3$) is not valid, which explains a poorer model fit in Fig. 4 compared to that of the modified Clift-Gauvin model. It should be noted that both models have the same number of the fitting parameters. This further demonstrates the importance of viscosity under our experimental conditions and justifies the use of the modified Clift-Gauvin model.

In our previous work [35], where gelatin samples were used as targets, the maximum penetration was measured with a reproducibility of about 30%. With such amount of scatter in the data, attributed to possible sample inhomogeneity and drying, the Poncelet model showed a reasonable agreement with the experiment. In the present study, drying was not an issue for the mineral-oil based gels and the scatter in the penetration data has been greatly reduced, which made it possible to distinguish between different models.

Effect of gel concentration

The maximum and residual penetration depth data shown in Fig. 5 reveal that, similar to the macroscale observations [38], gels with higher polymer content resisted penetration better. For instance, for an impact velocity of about 500 m/s, steel particles penetrated to a normalized depth of 10 into the 40-%vol gel versus 15 for the 20-vol% gel. The data were analyzed following the same procedure as for the 40-vol% gel; viscosities and resistances were extracted from the penetration depths for each concentration. As one can see in Fig. 5, the modified Clift-Gauvin model offers a good agreement for all concentrations with a deviation at low velocities below $\sim 200 \text{ m/s}$, similarly to the 40% gel data shown in Fig. 4. Figure 6 shows the resistance and viscosity values. While the resistance varies linearly with polymer content, the viscosity follows a power law with an exponent of 1.8. The viscosity values can be compared to rheological measurements performed by Mrozek et al. at 1 Hz frequency and 1% strain [38]. In those measurements, the viscosity ranges from 2 to 10 kPa/s for 15% to 40% polymer content (see Fig. S4). These values are greater than the apparent impact viscosity at high strain rates, which is characteristic of shear-thinning fluids [56]. It is difficult to compare the

absolute values of the viscosity because of the great disparity in the strain rate between our experiment and the rheological measurements [38]; however, it is noteworthy that the low-rate viscosity follows a similar power law, with an exponent of 1.6.

Conclusions

We have investigated the penetration dynamics of steel microparticles into non-aqueous polymer gels under high-velocity impact. Particles were launched using a laser-induced particle impact test platform and penetration dynamics were captured in real time using high-speed imaging, yielding trajectories of individual particles as well as maximum and residual penetration depths. We have found that the Clift-Gauvin drag model for Newtonian fluids, modified by adding a resistance term, provides a good fit to experimental data for a range of particle sizes and impact velocities. We have also shown that the modified Clift-Gauvin model agrees better with the experimental data than the Poncelet model over a large velocity range. The model parameters, i.e., the resistance and viscosity values, were obtained for five polymer concentrations with a power-law concentration dependence observed for both parameters. We believe that our methodology may lead to a better understanding of the behavior of viscosity in gels on the microscale at extreme strain rates. Another avenue for future research would be to find out if the same model can describe both macro- and microscale impact experiments with the same gel. Several aspects of our experiment left outside the scope of the present work such as the elastic recoil of the gel and cavity dynamics open additional prospects for future studies. The observation of the cavity dynamics with high temporal and spatial resolution will guide numerical simulations of the complex behavior of gels under high-velocity impacts.

Acknowledgments

DV thanks Drs. Bianca Giovanardi and Anwar Koshakji for fruitful discussions. This material is based upon work supported by the U. S. Army Research Office through the Institute for Soldier Nanotechnologies, under Cooperative Agreement Number W911NF-18-2-0048. The authors have no competing interests to declare.

Additional image sequences can be found in the supplementary information (Figs 5-12). The data that support the findings of this work are available from the corresponding author upon request.

Conflict of interest

Conflict of Interest: The authors declare that they have no conflict of interest.

References

1. Christiansen EL, Nagy K, Lear DM, Prior TG (2009) Space station MMOD shielding. *Acta Astronaut* 65:921–929. <https://doi.org/10.1016/j.actaastro.2008.01.046>
2. Christiansen EL, Hyde JL, Bernhard RP (2004) Space Shuttle debris and meteoroid impacts. *Adv Sp Res* 34:1097–1103. <https://doi.org/10.1016/j.asr.2003.12.008>
3. Parsi M, Najmi K, Najafifard F, et al (2014) A comprehensive review of solid particle erosion modeling for oil and gas wells and pipelines applications. *J Nat Gas Sci Eng* 21:850–873. <https://doi.org/10.1016/j.jngse.2014.10.001>
4. Pepi M, Squillacioti R, Pfluederer L, Phelps A (2012) Solid Particle Erosion Testing of Helicopter Rotor Blade Materials. *J Fail Anal Prev* 12:96–108. <https://doi.org/10.1007/s11668-011-9531-3>
5. Tilly GP (1969) Erosion caused by airborne particles. *Wear* 14:63–79. [https://doi.org/10.1016/0043-1648\(69\)90035-0](https://doi.org/10.1016/0043-1648(69)90035-0)
6. Moridi A, Hassani-Gangaraj SM, Guagliano M, Dao M (2014) Cold spray coating: review of material systems and future perspectives. *Surf Eng* 30:369–395. <https://doi.org/10.1179/1743294414Y.0000000270>
7. Kendall M, Mitchell T, Wrighton-Smith P (2004) Intradermal ballistic delivery of micro-particles into excised human skin for pharmaceutical applications. *J Biomech* 37:1733–41. <https://doi.org/10.1016/j.jbiomech.2004.01.032>
8. Hill PF, Edwards DP, Bowyer GW (2001) Small Fragment Wounds: Biophysics, Pathophysiology and

- Principles of Management. *J R Army Med Corps* 147:41–51. <https://doi.org/10.1136/jramc-147-01-04>
9. Hisley DM, Gurganus JC, Drysdale AW (2011) Experimental Methodology Using Digital Image Correlation to Assess Ballistic Helmet Blunt Trauma. *J Appl Mech* 78:051022. <https://doi.org/10.1115/1.4004332>
 10. Salisbury CP, Cronin DS (2009) Mechanical properties of ballistic gelatin at high deformation rates. *Exp Mech* 49:829–840. <https://doi.org/10.1007/s11340-008-9207-4>
 11. Miller DL, Smith NB, Bailey MR, et al (2012) Overview of therapeutic ultrasound applications and safety considerations. *J Ultrasound Med* 31:623–634. <https://doi.org/10.7863/jum.2012.31.4.623>
 12. Mancia L, Vlasisavljevich E, Xu Z, Johnsen E (2017) Predicting Tissue Susceptibility to Mechanical Cavitation Damage in Therapeutic Ultrasound. *Ultrasound Med Biol* 43:1421–1440. <https://doi.org/10.1016/j.ultrasmedbio.2017.02.020>
 13. Lee T, Luo W, Li Q, et al (2017) Laser-Induced Focused Ultrasound for Cavitation Treatment: Toward High-Precision Invisible Sonic Scalpel. *Small* 13:1–10. <https://doi.org/10.1002/smll.201701555>
 14. Gama BA, Lopatnikov SL, Gillespie JW (2004) Hopkinson bar experimental technique: A critical review. *Appl. Mech. Rev.* 57:223
 15. Richler D, Rittel D (2014) On the Testing of the Dynamic Mechanical Properties of Soft Gelatins. *Exp Mech* 54:805–815. <https://doi.org/10.1007/s11340-014-9848-4>
 16. Song B, Chen W (2004) Dynamic stress equilibration in split Hopkinson pressure bar tests on soft materials. *Exp Mech* 44:300–312. <https://doi.org/10.1177/0014485104041543>
 17. Toyoda Y, Gupta YM (2014) Shockless and shock wave compression of ballistic gel to 1.3 GPa. *J Appl Phys* 116:. <https://doi.org/10.1063/1.4898679>
 18. Estrada JB, Barajas C, Henann DL, et al (2018) High strain-rate soft material characterization via inertial cavitation. *J Mech Phys Solids* 112:291–317. <https://doi.org/10.1016/j.jmps.2017.12.006>
 19. Panzer MB, Myers BS, Capehart BP, Bass CR (2012) Development of a finite element model for blast brain injury and the effects of CSF cavitation. *Ann Biomed Eng* 40:1530–1544.

<https://doi.org/10.1007/s10439-012-0519-2>

20. Marjoribanks RS, Dille C, Schoenly JE, et al (2012) Ablation and thermal effects in treatment of hard and soft materials and biotissues using ultrafast-laser pulse-train bursts. *Photonics Lasers Med* 1:155–169. <https://doi.org/10.1515/plm-2012-0020>
21. Lee J-H, Veysset D, Singer JP, et al (2012) High strain rate deformation of layered nanocomposites. *Nat Commun* 3:1164. <https://doi.org/10.1038/ncomms2166>
22. Veysset D, Hsieh AJ, Kooi S, et al (2016) Dynamics of supersonic microparticle impact on elastomers revealed by real-time multi-frame imaging. *Sci Rep* 6:25577. <https://doi.org/10.1038/srep25577>
23. Hassani-Gangaraj M, Veysset D, Nelson KA, Schuh CA (2018) In-situ observations of single microparticle impact bonding. *Scr Mater* 145:9–13. <https://doi.org/10.1016/j.scriptamat.2017.09.042>
24. Hassani-Gangaraj M, Veysset D, Nelson KA, Schuh CA (2017) Melting Can Hinder Impact-Induced Adhesion. *Phys Rev Lett* 119:175701. <https://doi.org/10.1103/PhysRevLett.119.175701>
25. Xie W, Alizadeh-Dehkarghani A, Chen Q, et al (2017) Dynamics and extreme plasticity of metallic microparticles in supersonic collisions /639/166/988 /639/301/1023/1026 /639/301/930/12 /128 article. *Sci Rep* 7:1–9. <https://doi.org/10.1038/s41598-017-05104-7>
26. Hassani-Gangaraj M, Veysset D, Nelson KA, Schuh CA (2019) Impact-Bonding with Aluminum, Silver, and Gold Microparticles: Toward Understanding the Role of Native Oxide Layer. *Appl Surf Sci* 476:528–532. <https://doi.org/10.1016/j.apsusc.2019.01.111>
27. Hassani-Gangaraj M, Veysset D, Nelson KA, Schuh CA (2018) Melt-driven erosion in microparticle impact. *Nat Commun* 9:5077. <https://doi.org/10.1038/s41467-018-07509-y>
28. Veysset D, Hsieh AJ, Kooi SE, Nelson KA (2017) Molecular influence in high-strain-rate microparticle impact response of poly(urethane urea) elastomers. *Polymer* 123:30–38. <https://doi.org/10.1016/j.polymer.2017.06.071>
29. Hsieh AJ, Veysset D, Miranda DF, et al (2018) Molecular influence in the glass/polymer interface design: The role of segmental dynamics. *Polymer* 146:222–229.

- <https://doi.org/10.1016/j.polymer.2018.05.034>
30. Wu Y-CM, Hu W, Sun Y, et al (2019) Unraveling the high strain-rate dynamic stiffening in select model polyurethanes – the role of intermolecular hydrogen bonding. *Polymer* 168:218–227. <https://doi.org/10.1016/j.polymer.2019.02.038>
31. Sun Y, Wu Y-CM, Veysset D, et al (2019) Molecular dependencies of dynamic stiffening and strengthening through high strain rate microparticle impact of polyurethane and polyurea elastomers. *Appl Phys Lett* 115:093701. <https://doi.org/10.1063/1.5111964>
32. Lee J-H, Loya PE, Lou J, Thomas EL (2014) Dynamic mechanical behavior of multilayer graphene via supersonic projectile penetration. *Science* 346:1092–1096. <https://doi.org/10.1126/science.1258544>
33. Xie W, Tadepalli S, Park SH, et al (2018) Extreme Mechanical Behavior of Nacre-Mimetic Graphene-Oxide and Silk Nanocomposites. *Nano Lett* 18:987–993. <https://doi.org/10.1021/acs.nanolett.7b04421>
34. Hyon J, Lawal O, Fried O, et al (2018) Extreme Energy Absorption in Glassy Polymer Thin Films by Supersonic Micro-projectile Impact. *Mater Today* 21:817–824. <https://doi.org/10.1016/j.mattod.2018.07.014>
35. Veysset D, Kooi SE, Maznev AA, et al (2018) High-velocity micro-particle impact on gelatin and synthetic hydrogel. *J Mech Behav Biomed Mater* 86:71–76. <https://doi.org/10.1016/j.jmbbm.2018.06.016>
36. Liu K, Jiang M, Wu Z, et al (2019) A mechanical model for spherical fragments penetrating gelatine. *Int J Impact Eng* 131:27–38. <https://doi.org/10.1016/j.ijimpeng.2019.04.022>
37. Clift R, Gauvin WH (1971) Motion of entrained particles in gas streams. *Can J Chem Eng* 49:439–448. <https://doi.org/10.1002/cjce.5450490403>
38. Mrozek RA, Leighliter B, Gold CS, et al (2015) The relationship between mechanical properties and ballistic penetration depth in a viscoelastic gel. *J Mech Behav Biomed Mater* 44:109–120. <https://doi.org/10.1016/j.jmbbm.2015.01.001>
39. Hassani-Gangaraj M, Veysset D, Nelson KA, Schuh CA (2016) Supersonic Impact of Metallic Micro-

particles. arXiv:161208081

40. Al Khalil M, Frissane H, Taddei L, et al (2019) SPH-based method to simulate penetrating impact mechanics into ballistic gelatin: Toward an understanding of the perforation of human tissue. *Extrem Mech Lett* 29:100479. <https://doi.org/10.1016/j.eml.2019.100479>
41. Meng S, Taddei L, Lebaal N, et al (2020) Modeling micro-particles impacts into ballistic gelatine using smoothed particles hydrodynamics method. *Extrem Mech Lett* 39:100852. <https://doi.org/10.1016/j.eml.2020.100852>
42. Akers B, Belmonte A (2006) Impact dynamics of a solid sphere falling into a viscoelastic micellar fluid. *J Nonnewton Fluid Mech* 135:97–108. <https://doi.org/10.1016/j.jnnfm.2006.01.004>
43. Ansley RW, Smith TN (1967) Motion of spherical particles in a Bingham plastic. *AIChE J* 13:1193–1196. <https://doi.org/10.1002/aic.690130629>
44. Luu L-H, Forterre Y (2009) Drop impact of yield-stress fluids. *J Fluid Mech* 632:301–327. <https://doi.org/10.1017/S0022112009007198>
45. Ovarlez G, Cohen-Addad S, Krishan K, et al (2013) On the existence of a simple yield stress fluid behavior. *J Nonnewton Fluid Mech* 193:68–79. <https://doi.org/10.1016/j.jnnfm.2012.06.009>
46. Tabuteau H, Coussot P, de Bruyn JR (2007) Drag force on a sphere in steady motion through a yield-stress fluid. *J Rheol (N Y N Y)* 51:125–137. <https://doi.org/10.1122/1.2401614>
47. De Bruyn JR, Walsh AM (2004) Penetration of spheres into loose granular media. *Can J Phys* 82:439–446. <https://doi.org/10.1139/p04-025>
48. Goossens WRA (2019) Review of the empirical correlations for the drag coefficient of rigid spheres. *Powder Technol* 352:350–359. <https://doi.org/10.1016/j.powtec.2019.04.075>
49. Yoshitake Y, Mitani S, Sakai K, Takagi K (2008) Surface tension and elasticity of gel studied with laser-induced surface-deformation spectroscopy. *Phys Rev E - Stat Nonlinear, Soft Matter Phys* 78:1–7. <https://doi.org/10.1103/PhysRevE.78.041405>
50. Nakamura T, Hattori M, Kawasaki H, et al (1996) Surface tension of the polymer network of a gel.

Phys Rev E - Stat Physics, Plasmas, Fluids, Relat Interdiscip Top 54:1663–1668

51. Jin Y, Mai R, Wu C, et al (2018) Comparison of ballistic impact effects between biological tissue and gelatin. *J Mech Behav Biomed Mater* 78:292–297. <https://doi.org/10.1016/j.jmbbm.2017.11.033>
52. Liu M, Hwang HY, Tao H, et al (2012) Terahertz-field-induced insulator-to-metal transition in vanadium dioxide metamaterial. *Nature* 1–4. <https://doi.org/10.1038/nature11231>
53. Dehn J (1987) A unified theory of penetration. *Int J Impact Eng* 5:239–248. [https://doi.org/10.1016/0734-743X\(87\)90041-8](https://doi.org/10.1016/0734-743X(87)90041-8)
54. Liu L, Fan Y, Li W, Liu H (2012) Cavity dynamics and drag force of high-speed penetration of rigid spheres into 10wt% gelatin. *Int J Impact Eng* 50:68–75. <https://doi.org/10.1016/j.ijimpeng.2012.06.004>
55. Segletes SB (2008) Modeling the Penetration Behavior of Rigid Spheres Into Ballistic Gelatin. ART-TR-4393
56. Cross MM (1979) Relation between viscoelasticity and shear-thinning behaviour in liquids. *Rheol Acta* 18:609–614. <https://doi.org/10.1007/BF01520357>

Figure captions

Fig. 1 Laser-induced particle impact test platform. A laser pulse ablates a thin gold film, which causes expansion of a polyurea film and particle acceleration toward the gel target. The impact events are observed using a microscope and a high-speed camera.

Fig. 2 Image sequences showing particle impacts, with different particle diameters ((a) 20 and (b) 13 μm), on 40-vol% sample at (a) 215 m/s and (b) 630 m/s. The time delay relative to the first frame is shown at the top of the image. The exposure time for all images is 5 ns. Images are cropped from the original size.

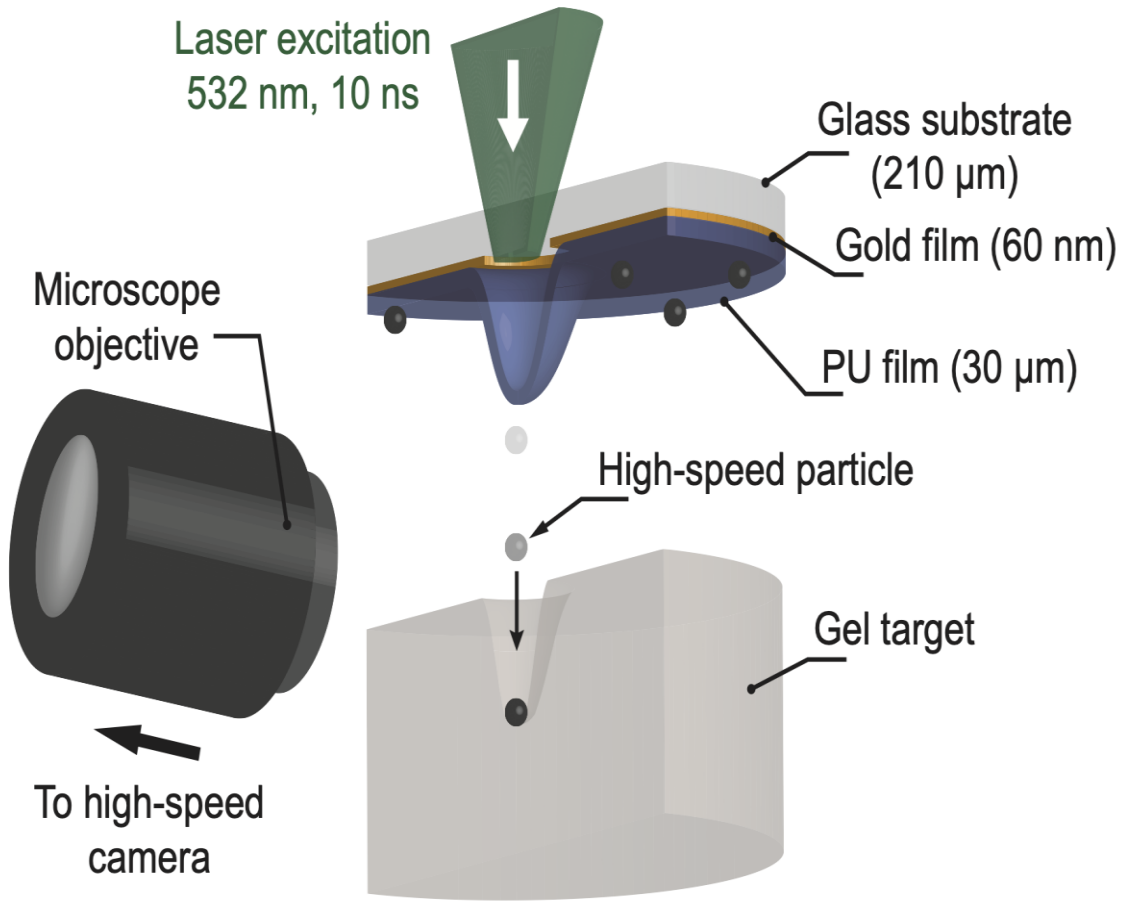
Fig. 3 (a) Penetration trajectories for three impact velocities on a 40-vol% sample. The modeled trajectories are represented by solid lines. (b) Normalized penetration depths as a function of impact velocity. The colors reflect the particle diameters.

Fig. 4 Experimental and fitted normalized maximum penetrations as a function on impact velocity for the 40-vol% sample, showing a better fit for the modified Clift-Gauvin model compared to the Poncelet model.

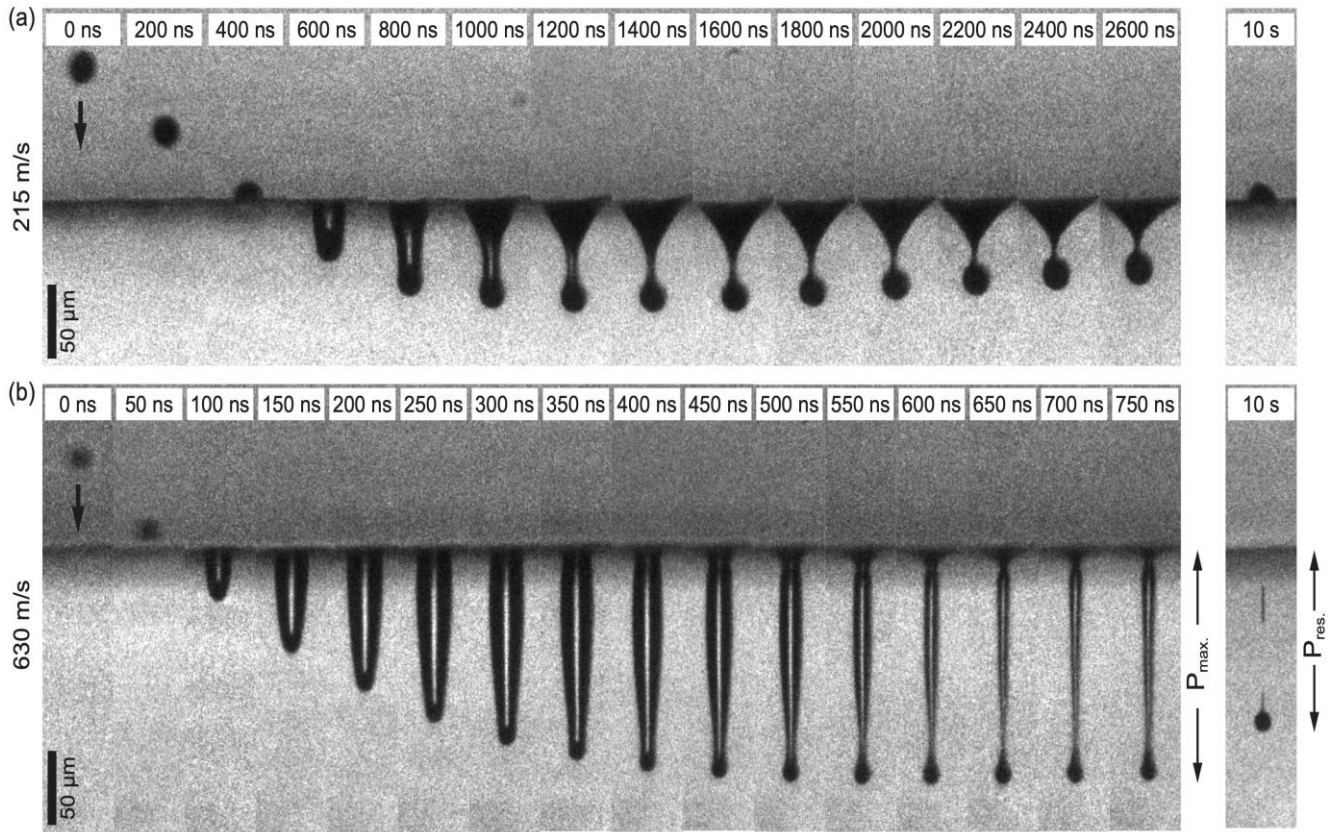
Fig. 5 Experimental and fitted (modified Clift-Gauvin model) normalized maximum and residual penetration as a function of impact velocity for different polymer contents. The 40-vol%-sample data and fits are shown in Fig. 4.

Fig. 6 (a) Fitted yield resistance and (b) fitted viscosity as a function of polymer concentration C . The resistance and viscosity dependences on concentration were fitted with a power law (dotted line).

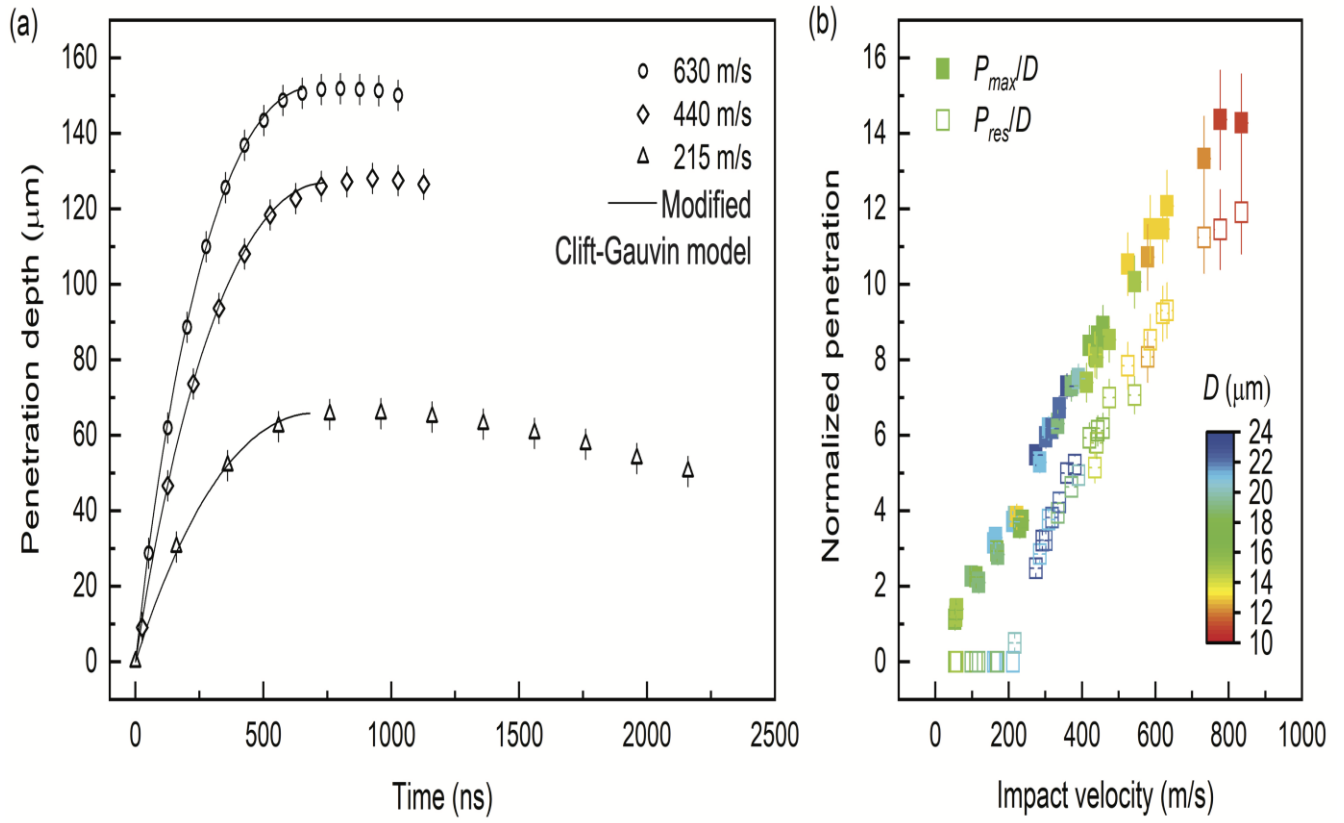
Author accepted manuscript



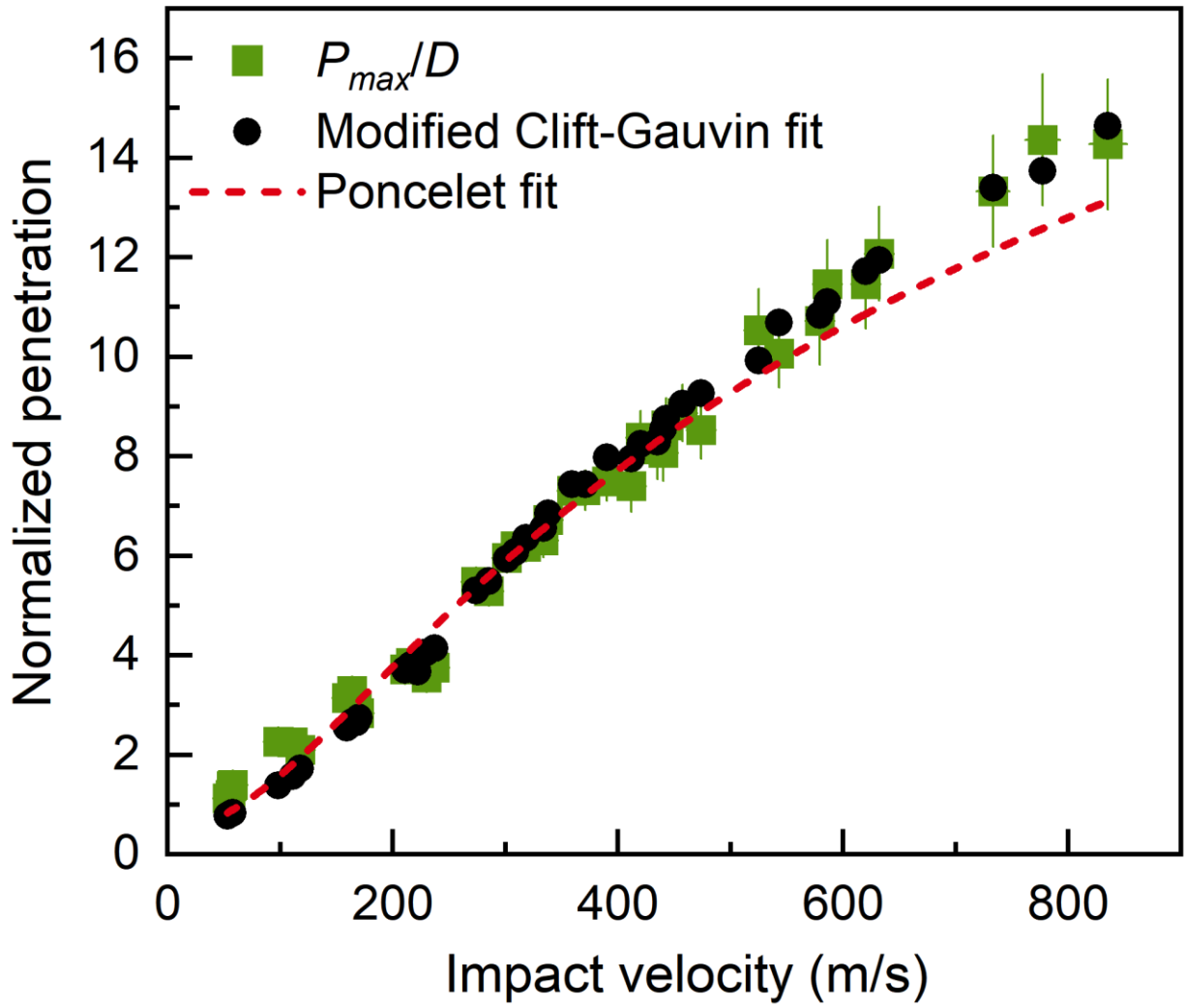
Author accepted



Author accepted



Author accepted



Author ac

